Available online at www.sciencedirect.com
SCIENCE DIRECT®
Journal of Power Sources 138 (2004) 162–173
JOURNAL OF POWER SOURCES
www.elsevier.com/locate/jpowsour

Sol–gel coatings to reduce oxide growth in interconnects used for solid oxide fuel cells

Wei Qu[a], Jian Li[a], Douglas G. Ivey[b]*

[a] *Fuel Cell Energy, Calgary, Alta., Canada T2B 3R2*
[b] *Department of Chemical and Materials Engineering, University of Alberta, Edmonton, Alta., Canada T6G 2G6*

Received 12 June 2004; accepted 24 June 2004
Available online 8 September 2004

Abstract

Ferritic stainless steels (16–18 wt.% Cr) can be used as interconnects for solid oxide fuel cells (SOFC) that operate at lower temperatures, i.e., <800 °C. Long-term reliability is a concern; however, as oxidation of the steel can occur readily at elevated temperatures leading to the formation of Cr_2O_3 and Cr–Mn spinel ($(Cr,Mn)_3O_4$). The aim of this work was to reduce oxide growth, in particular, the Cr_2O_3 phase, through the application of Y/Co and Ce/Co sol–gel coatings. Oxide growth was characterized using X-ray diffraction (XRD), scanning electron microscopy (SEM) and transmission electron microscopy (TEM). Coatings containing Y/Co provided the best resistance, producing Cr_2O_3 oxide layers more than 3 times thinner than for uncoated steels.

Keywords: Solid oxide fuel cells; Interconnects; Coatings; Electron microscopy; X-ray diffraction

1. Introduction

Anode-supported, planar solid oxide fuel cells (SOFCs) have electrolytes which are typically <20 μm thick, and in many cases <10 μm thick, permitting operation at temperatures <800 °C. Multiple planar SOFCs are stacked in series, to achieve sufficient voltages for practical applications, necessitating the use of interconnects to electronically connect anodes and cathodes to one another. In addition to being electronically conducting, interconnects must be easily fabricated, be stable at operating temperatures, have similar thermal expansion coefficients to other fuel cell components, have low ionic conductivity and be impermeable to fuel and oxidizing gases [1,2].

Candidate interconnect materials consist of two major types, electronically conductive oxides, such as $LaCrO_3$ and related ceramics, and oxidation resistant metallic alloys, such as ferritic stainless steels [1–4]. Ferritic stainless steels have many advantages compared with their ceramic counterparts, including reasonable mechanical stability, much higher thermal and electronic conductivities, little porosity, ease of fabrication and significantly lower cost. Although not suitable for high temperature fuel cells (900–1000 °C), they may be used for lower temperature anode-supported cells. Long-term reliability in fuel cell environments remains a concern; however, as the temperatures employed are pushing the limits of the steel.

Ferritic stainless steels form a protective oxide layer (primarily Cr_2O_3 with Cr–Mn spinel $(Cr,Mn)_3O_4$) on the surface. According to [5], the spinel phase is reasonably conducting, with a reported resistivity of ∼5 Ω cm at 750 °C. Cr_2O_3 is considered to be a poorer conductor; resistivities as low as $\sim 10^4$ Ω cm at the same temperature have been reported [5], although other references put the resistivity at closer to 100 Ω cm [6,7]. Interconnects are usually characterized in terms of an area specific resistance (ASR), which is just the product of the materials' electrical resistivity and its thickness. As a rule of thumb, an ASR value of 0.1 Ω cm^2 is considered to be the upper limit for fuel operation, in order

* Corresponding author. Tel.: +1 780 492 2957; fax.: +1 780 492 2881.
E-mail address: doug.ivey@ualberta.ca (D.G. Ivey[b]).

0378-7753/$ – see front matter © 2004 Elsevier B.V. All rights reserved.
doi:10.1016/j.jpowsour.2004.06.063

to minimize Ohmic losses [8]. Since stainless steels have much lower resistivities than their oxides, the interconnect substrate can be neglected in calculating its ASR. Using the same type of reasoning, the oxide of concern is Cr_2O_3 and not the spinel phase. For a 10 μm thick Cr_2O_3 layer forming at 750 °C on both surfaces of the interconnect metal (assuming the lower resistivity value of ∼100 Ω cm), the ASR value would be 0.2 Ω cm^2, which exceeds the limiting value. The higher value of Cr_2O_3 resistivity would give a much larger ASR value.

Two approaches can be taken to try and improve the ASR of the interconnect, i.e., decrease the oxide (Cr_2O_3) thickness and/or increase its conductivity. In the first case, rare earth elements, such as Y, Zr, La, Hf and Ce, can be added to reduce the oxide growth rate and have the added benefit of improving oxide adhesion [8–13]. The mechanisms involved are not clear, but may be related to decreased internal stresses for adhesion and blocking of short circuit diffusion paths for reduced oxide growth. The second approach involves doping Cr_2O_3, which is a p-type semiconductor, with divalent ions, such as Ni^{2+} and Co^{2+} [8,14] to increase its conductivity. As an example, doping with 1% Ni can improve the conductivity of Cr_2O_3 by a factor of ∼80 at 950 °C [14].

The purpose of this study was to improve the ASR value of ferritic stainless steel interconnects, primarily through applications of coatings to reduce the oxide layer thickness. Sol–gel coatings, containing rare earth oxides (Y_2O_3 or CeO_2) and Co^{2+} ions (p-type dopant for Cr_2O_3), were applied to ferritic stainless steels. The samples were oxidized in air at 750 °C. Electrical measurements were not made; only microstructures were characterized using X-ray diffraction (XRD), scanning electron microscopy (SEM) and transmission electron microscopy (TEM).

2. Experimental methods

Ferritic stainless steel (type 430) sheets, approximately 1 mm thick, were sectioned into coupons ∼2.5 cm × ∼2.5 cm. The coupons were ultrasonically cleaned in a 2% Citranox solution for 15 min, followed by rinsing in deionized water, soaking in ethanol and then drying. Two sol–gel solutions were prepared. The Y–Co solution was prepared using yttrium nitrate ($Y(NO_3)_3{\cdot}6H_2O$) and 0.1M cobalt chloride hexahydrate ($CoCl_2{\cdot}6H_2O$), while the Ce–Co solution was prepared with cerium(III) chloride ($CeCl_3$) replacing the yttrium nitrate. Coatings were applied by dipping the coupons

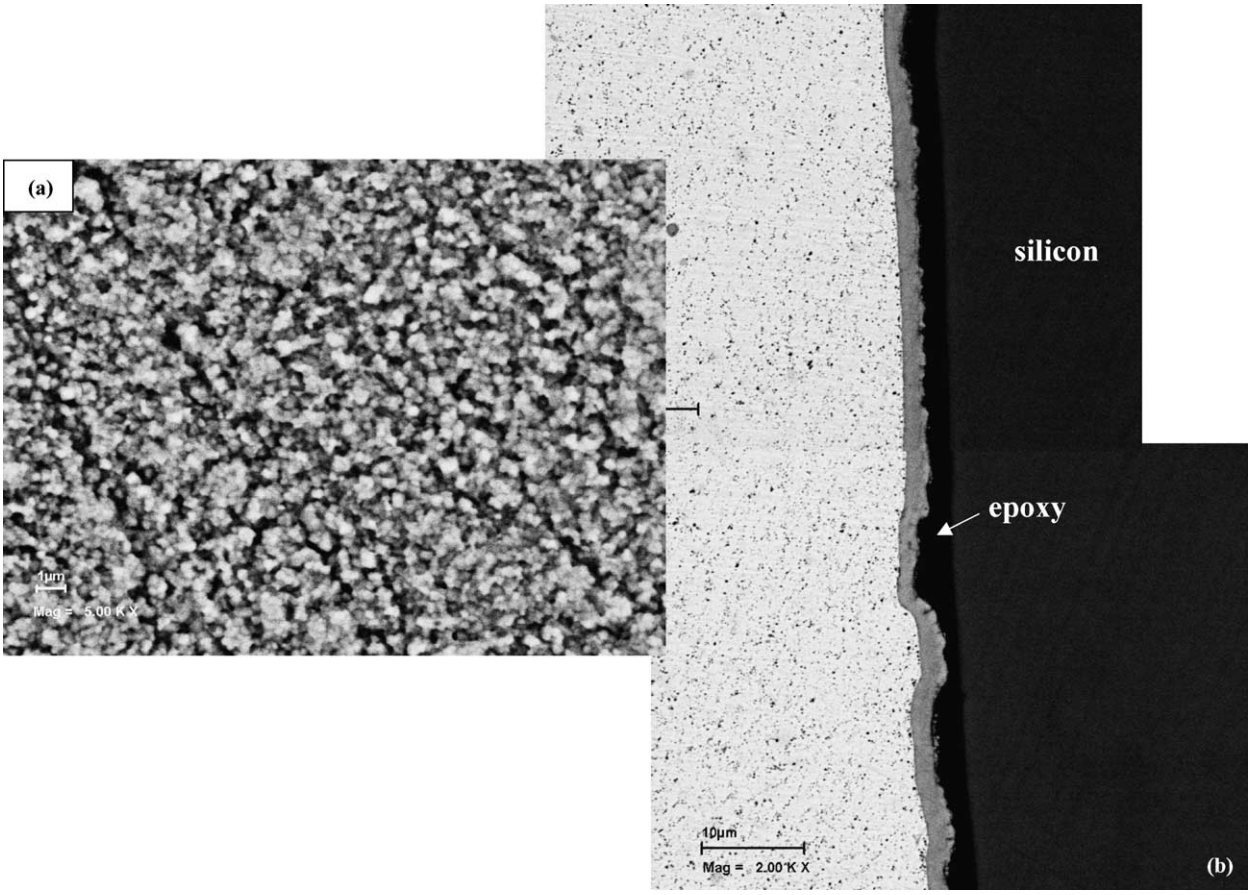

Fig. 1. SEM backscattered electron (BSE) images from a bare stainless steel sample annealed in air at 750 °C for 1000 h. (a) Plan view image of surface; (b) cross section image.

into the solutions and then drying in an oven at 150–180 °C. All samples, including reference stainless steel samples, were annealed in air at 750 °C for up to 1000 h.

Samples were examined by XRD, using a Rigaku Rotoflex rotating anode system, with a thin film camera attachment, to allow characterization of the oxide with minimal interference from the ferrite substrate. The filament voltage and current were set at 40 kV and 110 mA, respectively. Samples were scanned between 10 and 90° at a rate of 2° min^{-1} using an X-ray incidence angle of 2°.

Both plan view and cross section samples were examined by SEM. Cross section samples for SEM analysis were prepared using standard metallographic techniques. A piece, ~2 mm × 5 mm, was sectioned from an oxidized steel sample and glued to a piece of Si of the same size. The two pieces were then glued to additional Si pieces producing a "raft-like" structure. These rafts were polished with a series of increasingly finer grit SiC papers and finally 1 μm diamond paste. Polished samples were examined in a LEO 1450VP (variable pressure) SEM equipped with an Oxford Instruments ultra thin window (UTW) X-ray detector for energy dispersive X-ray (EDX) microanalysis.

Cross sections were prepared of selected samples for TEM analysis. As for SEM analysis, a raft containing one of the oxidized samples was prepared. Discs, 3 mm in diameter, were then machined from the raft-like structure using an ultrasonic disc cutter. Each disc was polished to a final thickness of 100–200 μm using 400 and 600 grit SiC abrasive papers. The disc was mechanically dimpled from both sides down to a final central thickness of <10 μm, using 3 μm and then 1 μm diamond polishing pastes. The purpose of this step was to remove most of the central material while maintaining a relatively thick outer rim to facilitate handling. The final step involved ion milling both sides of the central region to perforation, using Ar ions at an energy of 6 keV, a current of 0.6 mA per gun and an incident angle of 17° to the surface. After perforation, sputtering was continued at a lower energy (4 keV) and current (0.3 mA per gun) to minimize sputtering induced damage. Specimens were liquid nitrogen cooled during the entire ion milling process in an effort to reduce preferential sputtering effects. Samples were examined in a Tecnai F20 field emission gun (FEG) TEM/STEM, equipped with an EDAX Phoenix UTW X-ray detector.

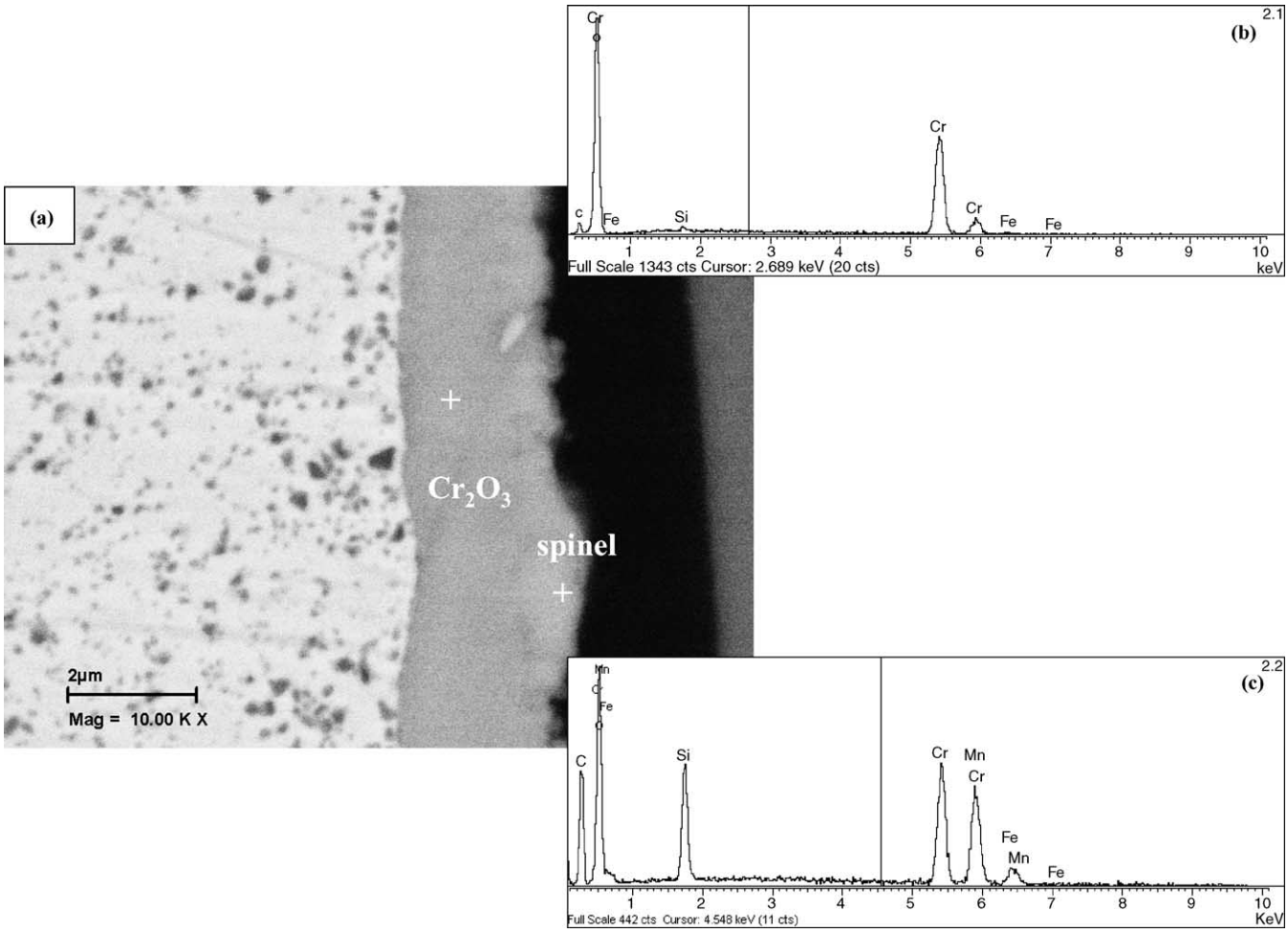

Fig. 2. (a) Higher magnification SEM BSE cross section image of sample shown in Fig. 1b. (b) EDX spectrum from inner oxide layer. (c) EDX spectrum from outer oxide layer.

3. Results and discussion

3.1. Uncoated stainless steel

Uncoated stainless steel coupons were used as a base line for comparison purposes. SEM plan view and cross section images of a sample annealed for 1000 h are shown in Fig. 1a–b, respectively. The oxide layer is continuous and fairly uniform in thickness. Imaging at higher magnification (Fig. 2a) indicates that there are two distinct surface oxides. The inner phase is Cr-rich (Fig. 2b) and more uniform in thickness, measuring between 2.0 and 2.6 μm, while the outer

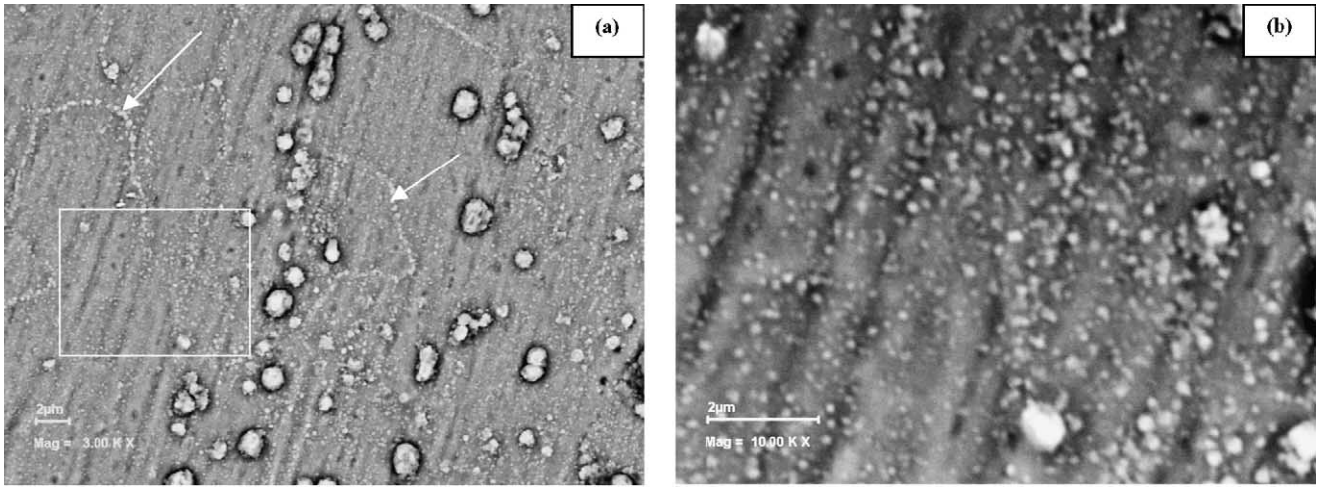

Fig. 3. SEM BSE images from a plan view specimen of Ce/Co sol–gel sample annealed at 750 °C for 1 h. Underlying ferrite grain boundaries are indicated by arrows. The region indicated by a square in (a) is magnified in (b).

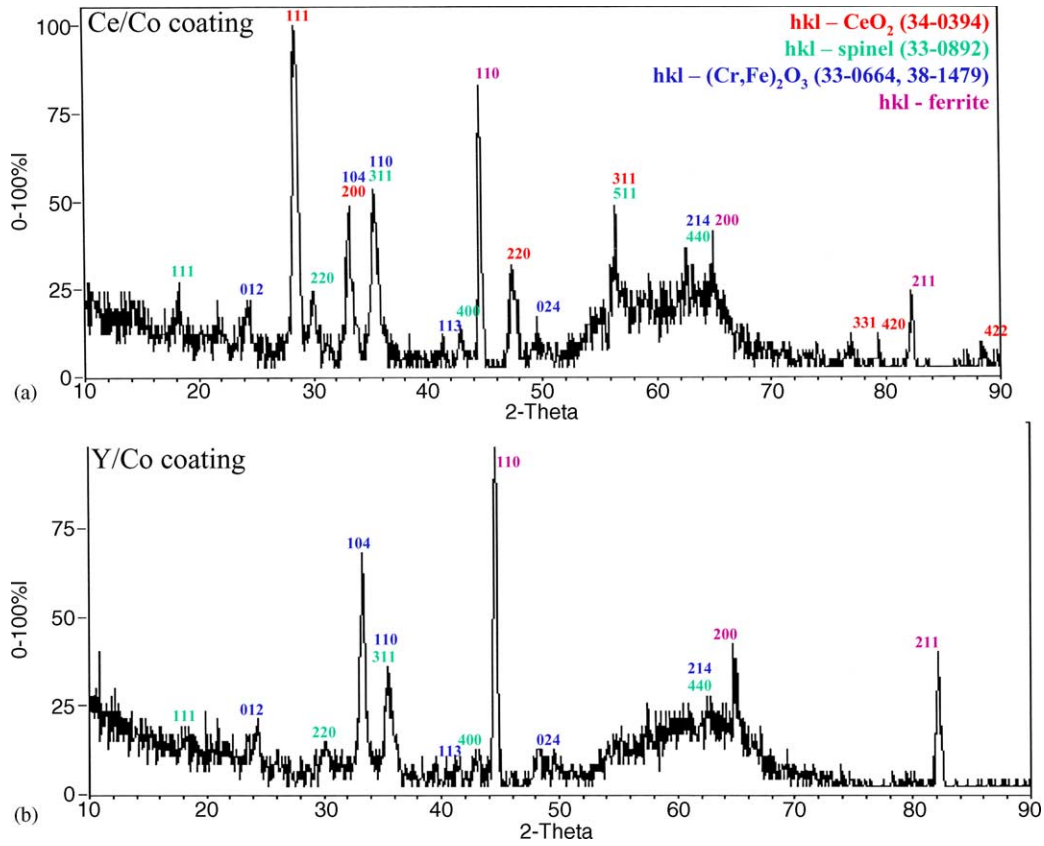

Fig. 4. (a) Indexed XRD spectrum from Ce/Co sol–gel sample annealed at 750 °C for 1 h. (b) Indexed XRD spectrum from Y/Co sol–gel sample annealed at 750 °C for 1 h.

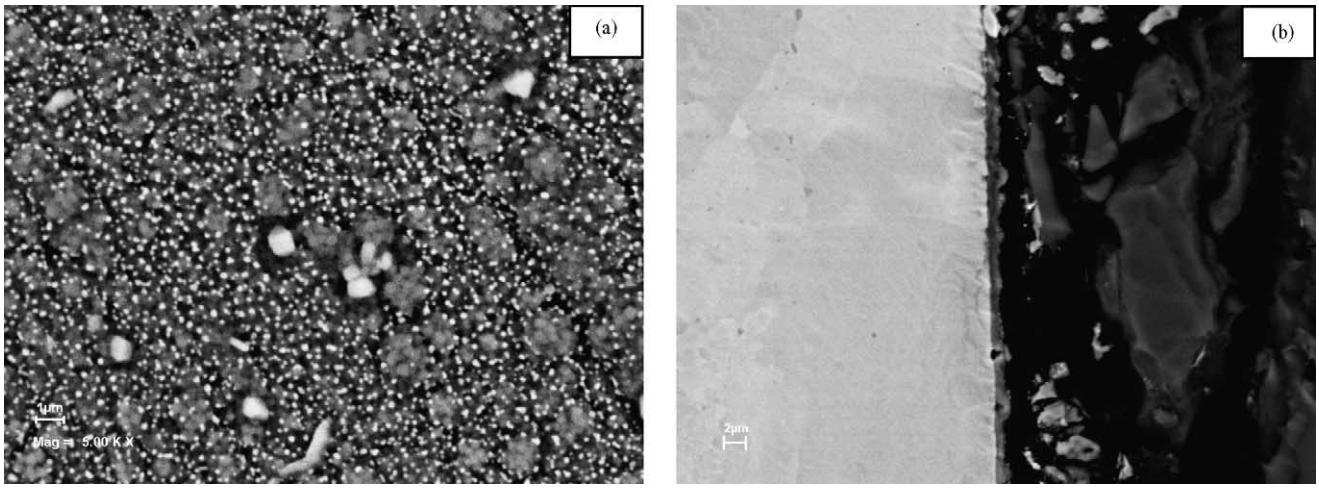

Fig. 5. SEM BSE images from Ce/Co sol–gel sample annealed for 500 h. (a) Plan view image of surface; (b) cross section image.

phase is Cr–Mn rich (Fig. 2c). Both phases contain Fe, which is likely due to partial substitution of Fe for the other transition metals. The identity of the oxides was confirmed by XRD analysis. The diffraction peaks were indexed as $(Cr,Mn)_3O_4$ spinel and Cr_2O_3, as would be expected. Iron forms an oxide (hexagonal Fe_2O_3 or hematite with a = 0.5036 nm and c = 1.3749 nm) with the same crystal structure and similar lattice parameters to Cr_2O_3 (a = 0.4959 nm and c = 1.3594 nm). The presence of Fe in the spinel phase is not surprising as many of the transition metals, e.g., Cr, Mn, Fe, Co, form cubic spinel phases, with lattice parameters ranging from ∼0.81 to 0.85 nm. The Si peak present in the EDX spectra, particularly Fig. 2c, is a polishing artefact that arises from the Si pieces used as filler material in cross section specimen preparation.

3.2. Ce/Co sol–gel coating

Coatings were initially heated to 750 °C for 1 h. The resulting layer thickness was difficult to measure, but was estimated from SEM cross sections to be ∼200 nm. SEM plan view images of this sample are shown in Fig. 3. It is apparent from Fig. 3 that the surface layer is quite thin, as the grain

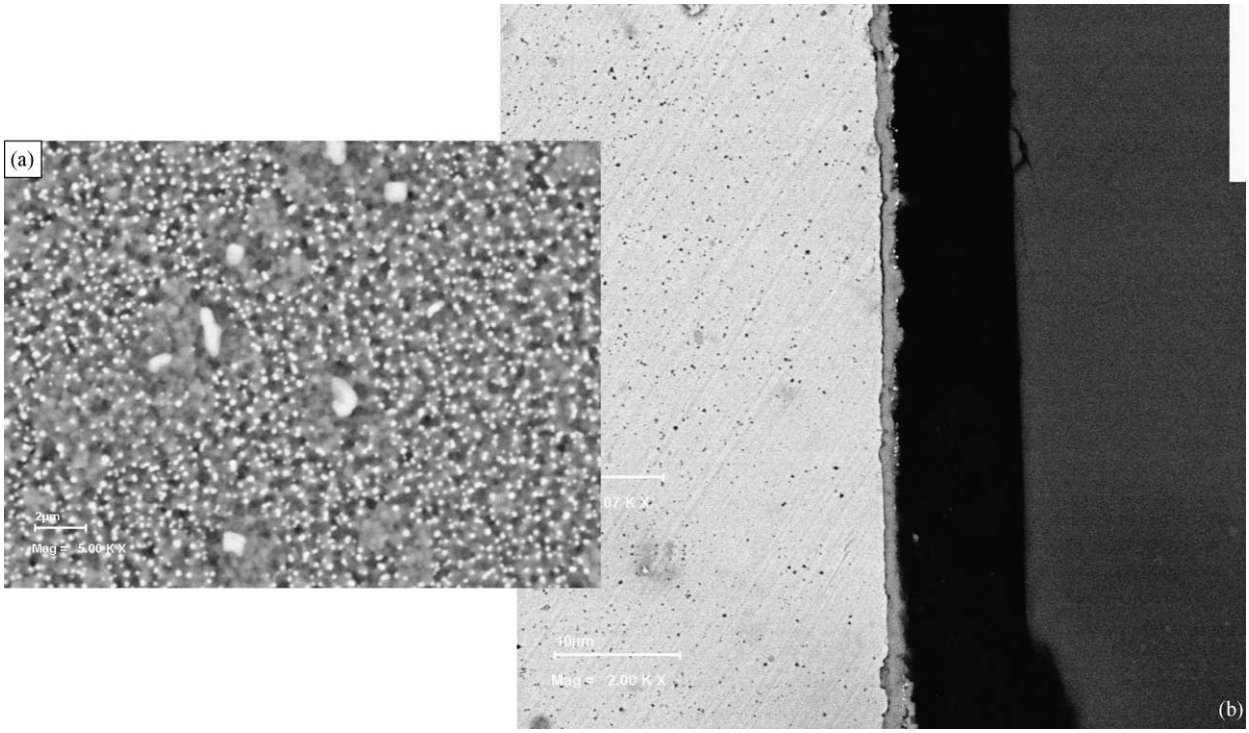

Fig. 6. SEM BSE images from Ce/Co sol–gel sample annealed for 1000 h. (a) Plan view image of surface; (b) cross section image.

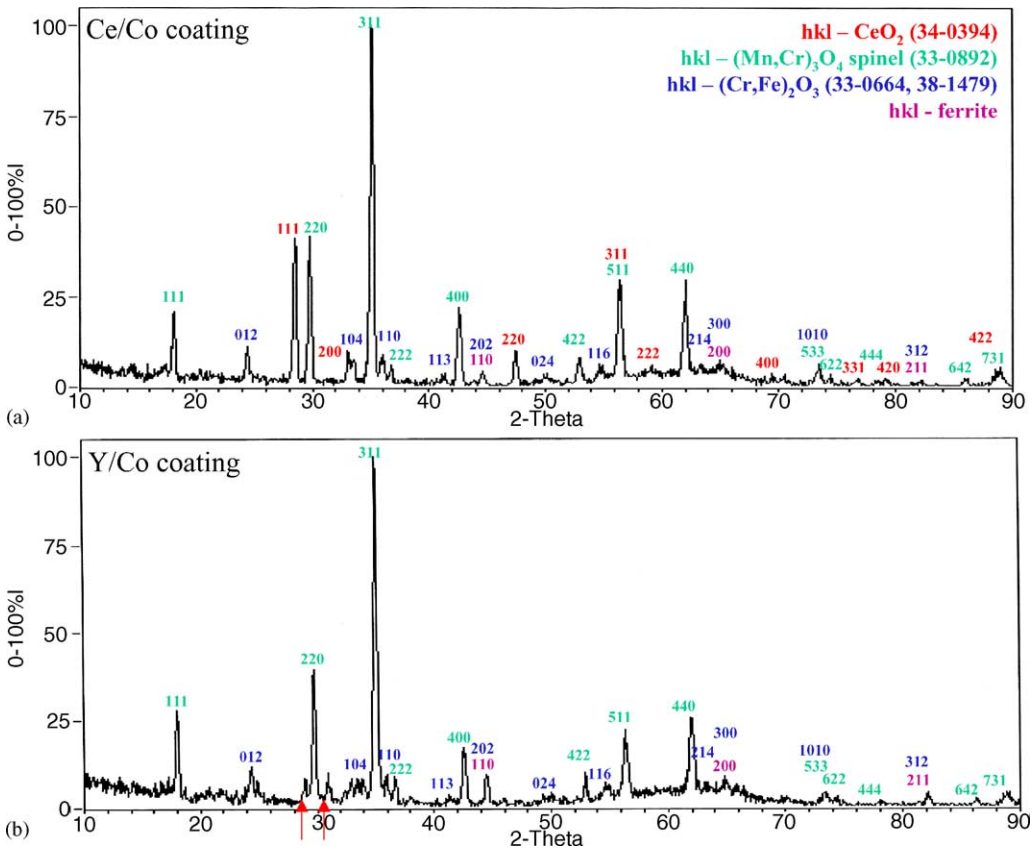

Fig. 7. (a) Indexed XRD spectrum from Ce/Co sol–gel sample annealed at 750 °C for 500 h. (b) Indexed XRD spectrum from Y/Co sol–gel sample annealed at 750 °C for 500 h.

boundaries from the ferrite substrate are visible. The grain boundaries are decorated with small, white particles (a few hundred nanometers in size or smaller), with additional particles scattered across the entire surface. The particles were difficult to analyze by EDX in the SEM, due to spatial resolution limitations, but were speculated and later confirmed (by XRD analysis) to be CeO_2 (Fig. 4). Larger white particles (up to several microns in size) were also present across the surface. These were Ce and O rich and again identified as CeO_2. No separate Co or Co-oxide phases were detected.

SEM images of samples annealed at 750 °C for 500 and 1000 h are shown in Figs. 5 and 6, respectively. As with the uncoated samples, two oxides are visible. The inner oxide is Cr-rich, while the outer oxide is Cr–Mn rich; XRD analysis confirmed these to be Cr_2O_3 and $(Cr,Mn)_3O_4$ (Fig. 7a). Separating the two phases is a line of white particles (Fig. 8a). EDX analysis (Fig. 8b) indicates that these are Ce- and O-rich and therefore likely CeO_2, which was confirmed by XRD (Fig. 7a) and TEM analysis (see below). The CeO_2 particles act as a marker indicating that oxygen is the primary diffuser in the formation of Cr_2O_3, while Mn and Fe along with some Cr diffuse to the surface in the formation of the spinel phase. This result appears to be in agreement with previous studies involving coatings with rare earth elements [7,12,13]. Cr_2O_3 growth on Cr-containing alloys is generally believed to be due to Cr outward diffusion along short circuit paths, e.g., grain boundaries. Therefore, the oxide forms at the oxide/gas interface. In the presence of rare earths, the process can be reversed with O anions becoming the dominant diffusing species as shown here. It is clear from the EDX spectra in Fig. 8 that Ce is only present in the CeO_2 particles and has not dissolved (at least within the detectability limit of EDX) into either the Cr_2O_3 or spinel phases. Previous work on a high Cr (26 wt.%) ferritic stainless steel has shown that sputtered CeO_2 layers react with Cr to produce $CeCrO_3$, although the oxidation temperature was much higher (900 °C) [15].

No Co-rich phases were detected by SEM or XRD analysis. It appears that Co has dissolved into the oxide phases, primarily the spinel phase. The presence of Co, at low concentrations, is difficult to identify by EDX because its Kα X-ray peak overlaps with the Kβ peak for Fe. There is, however, a small shoulder to the left of the Kβ peak for Fe (indicated by an arrow in Fig. 8c and d), confirming the presence of Co. Cobalt dissolution in Cr_2O_3 may be beneficial as a p-type dopant in Cr_2O_3, although this effect was not confirmed in the present work.

TEM analysis was used to confirm the identity of the CeO_2 phase. A bright field image of a cross section specimen taken from a sample annealed for 500 h is shown in Fig. 9, along with a Ce X-ray map and a representative microdiffraction

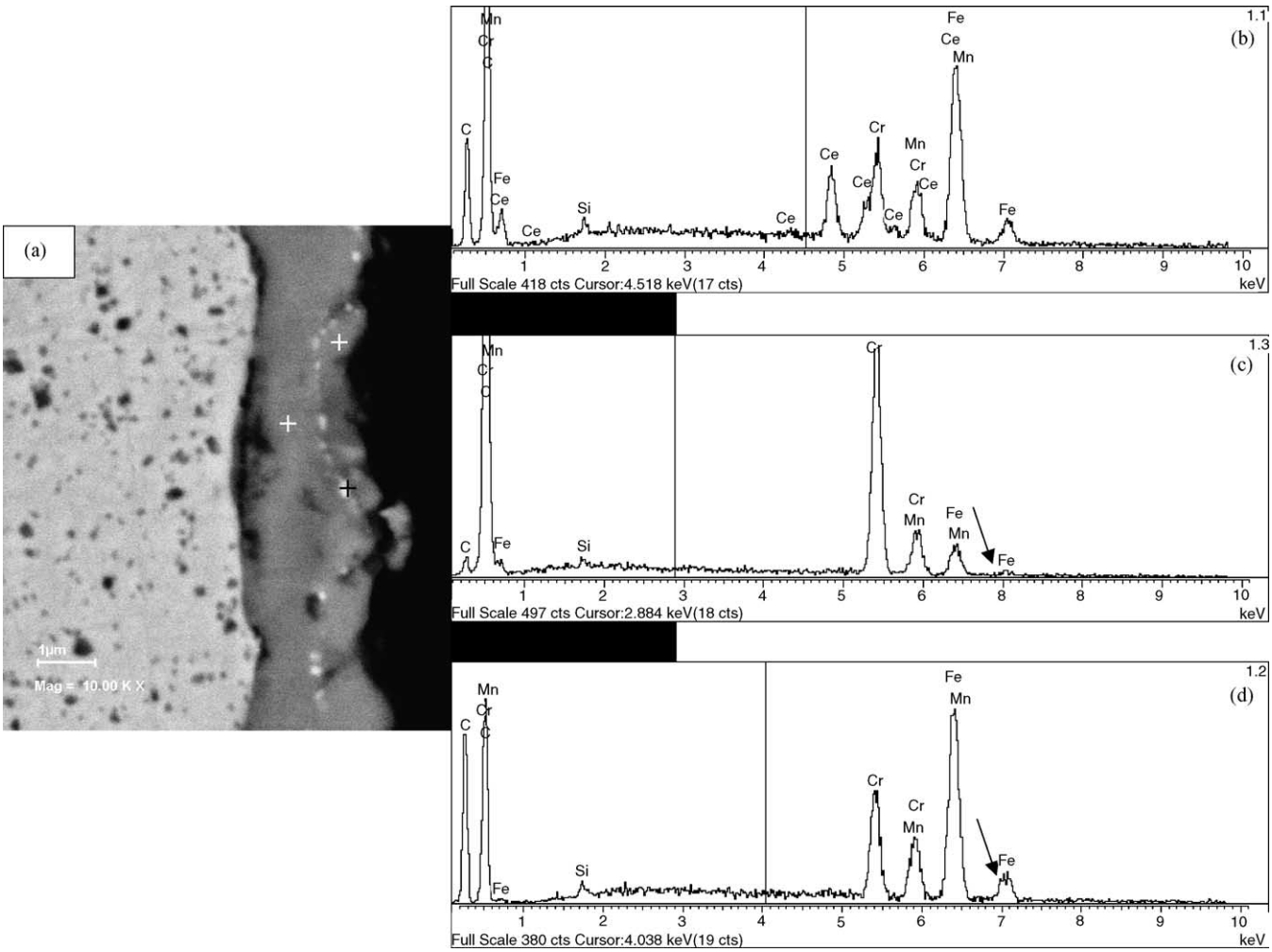

Fig. 8. (a) SEM BSE image from Ce/Co sol–gel sample annealed for 1000 h. (b) EDX spectrum from particles at interface between two oxides. (c) EDX spectrum from inner oxide layer. (d) EDX spectrum from outer oxide layer.

pattern from one of the Ce-rich grains. The pattern was indexed to CeO_2, which has a fluorite-type structure with a = 0.5411 nm.

The Cr_2O_3 layer is continuous, but somewhat more variable in thickness than for the uncoated steel. The thickness is <1.0 μm for the 500 h sample and varies from 1.0 to 1.5 μm for the 1000 h sample, which is about half the thickness for the uncoated steel. CeO_2 sol–gel coatings have been shown to significantly reduce the oxidation rate of Ni at temperatures below 1000 °C [9]. The effect is attributed to grain boundary segregation of CeO_2, providing a physical barrier to solid-state diffusion of the mobile species. For Ni, the activation energy for oxidation is ∼85 kJ mol^{-1} with CeO_2 (700–900 °C) compared with ∼180 kJ mol^{-1} for uncoated Ni. A similar mechanism could be operating here.

3.3. Y/Co sol–gel coating

Coatings were initially cured at 750 °C for 1 h. As with the Ce/Co material, the coating was quite thin (∼200 nm thick), which is apparent from the SEM image in Fig. 10. The ferrite grain boundaries are visible, but there is no preferential decoration with particles. The coating is continuous, with agglomerated regions dispersed on the surface. These have two size ranges—less than 500 nm and several microns. The agglomerated regions appear to be slightly Y-rich, relative to the rest of the coating, but no distinct Y_2O_3 particles or Y-rich phases were identified. Cobalt is dispersed evenly throughout the layer in Fig. 10. The only phases detected by XRD for all oxidation times (Fig. 4b–d) were Cr_2O_3 and Cr–Mn spinel, as well as the underlying ferrite substrate. If any Y–Cr oxides were present, they were below the detectability limit of XRD. Riffard et al. [11,13] detected Y–Cr oxides ($YCrO_3$ and $YCrO_4$) at the external surface for type 304 austenitic stainless steels, with yttria sol–gel coatings. Downham and Shendye [15] have identified $YCrO_3$ and Y_2O_3 phases in chromia scales for Y_2O_3 sputtered coatings on ferritic stainless steels. In both cases, the oxidation temperatures were significantly higher than the 750 °C utilized here—1000 °C for [11,13] and 900 °C for [15].

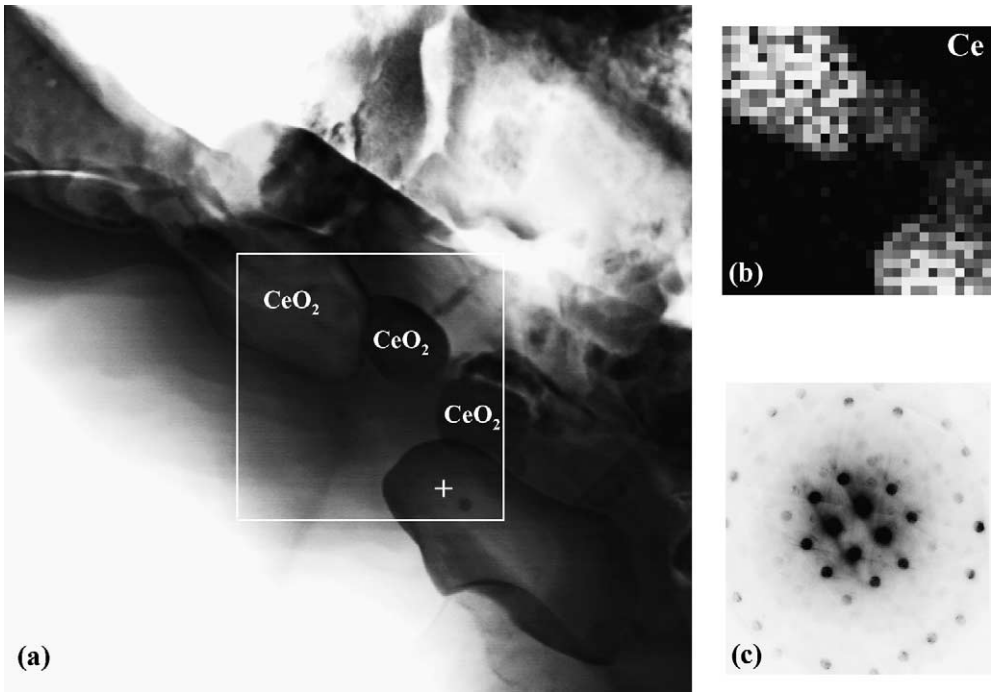

Fig. 9. (a) TEM BF image from cross section specimen of Ce/Co sol–gel sample annealed for 1000 h. (b) Ce X-ray map showing CeO_2 particles at interface between inner and outer oxide layers. (c) Representative microdiffraction pattern from indicated CeO_2 particle. Zone axis is [2 1 5].

SEM images for samples annealed for 500 and 1000 h are shown in Figs. 11 and 12, respectively. Two oxide layers, the inner Cr_2O_3 and outer spinel, are the only phases visible. Cr_2O_3 has a fine grain structure (<50 nm), which is evident from the STEM image in Fig. 13. The accompanying selected area diffraction (SAD) pattern in Fig. 14 confirms the polycrystalline nature of Cr_2O_3. No Co was detected in the Cr_2O_3, while low levels of Y were present throughout as indicated by the X-ray linescan in Fig. 13b. Closer inspection of the Y linescan (Fig. 13c) shows that Y levels are higher at the Cr_2O_3 grain boundaries. This result suggests that the reduced oxide growth rate may be due in part to Y segregation to grain boundaries [13] restricting Cr outward diffusion through Cr_2O_3. The spinel phase contains a significant amount of Co with virtually no Y (Fig. 14).

The Cr_2O_3 layer is variable in thickness, but continuous (as with uncoated and Ce/Co coated steel). The thickness is generally <1 μm, even for an annealing time of 1000 h; however, there are places on the surface where the Y/Co coating has scratched off prior to oxidation (Fig. 15). The oxide layer

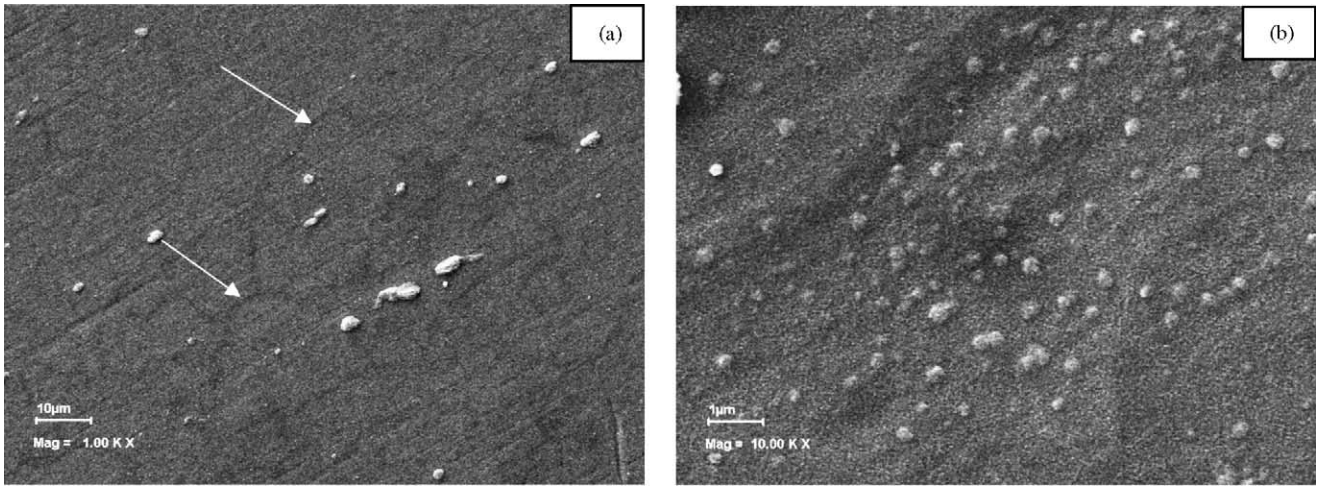

Fig. 10. SEM BSE images from a plan view specimen of an Y/Co sol–gel sample annealed at 750 °C for 1 h. Ferrite grain boundaries are indicated by the arrows.

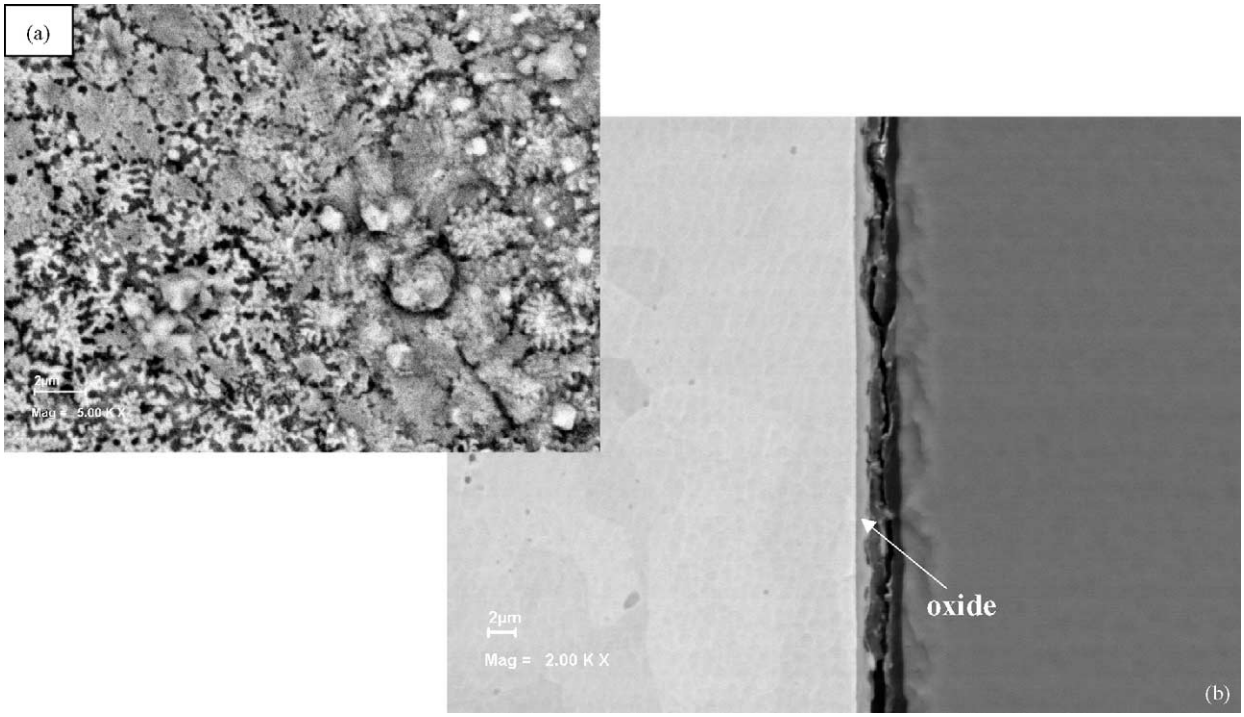

Fig. 11. SEM BSE images from Y/Co sol–gel sample annealed for 500 h. (a) Plan view image of surface; (b) cross section image.

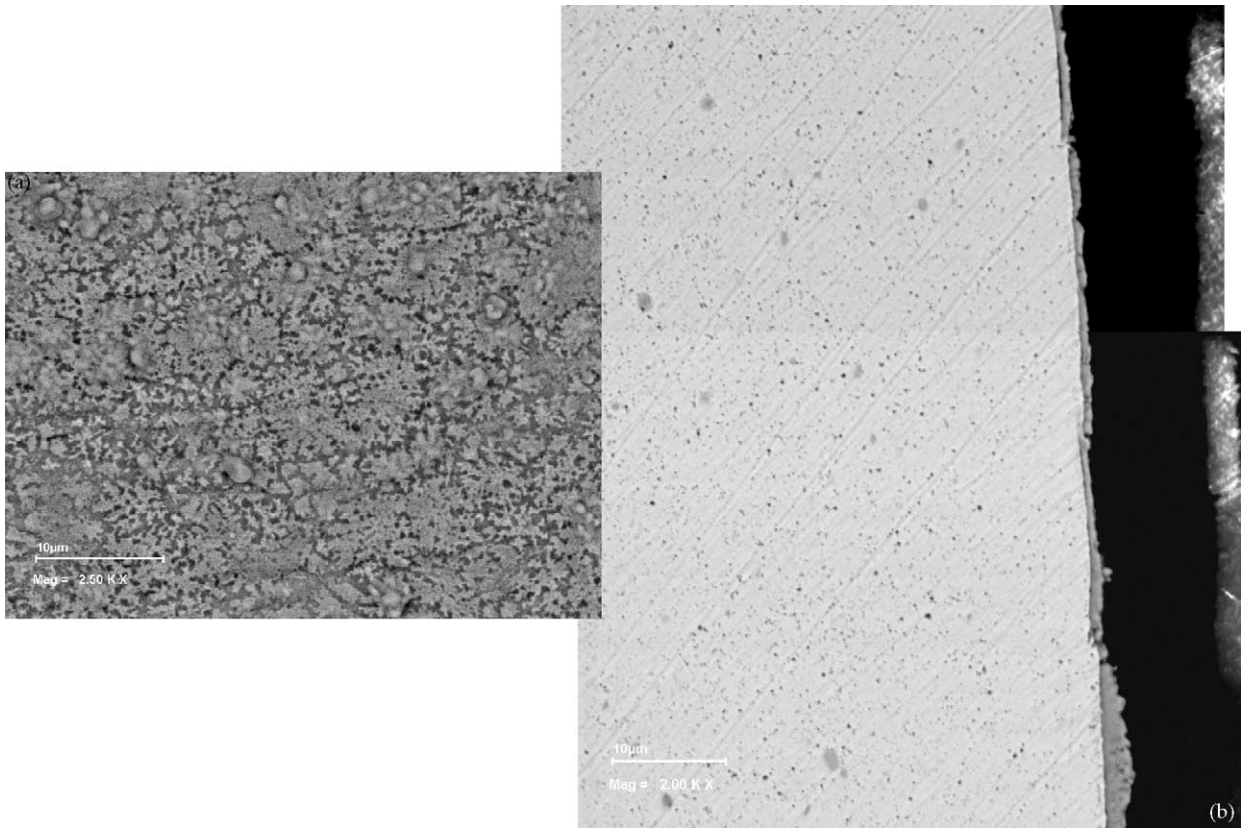

Fig. 12. SEM BSE images from Y/Co sol–gel sample annealed for 1000 h. (a) Plan view image of surface; (b) cross section image.

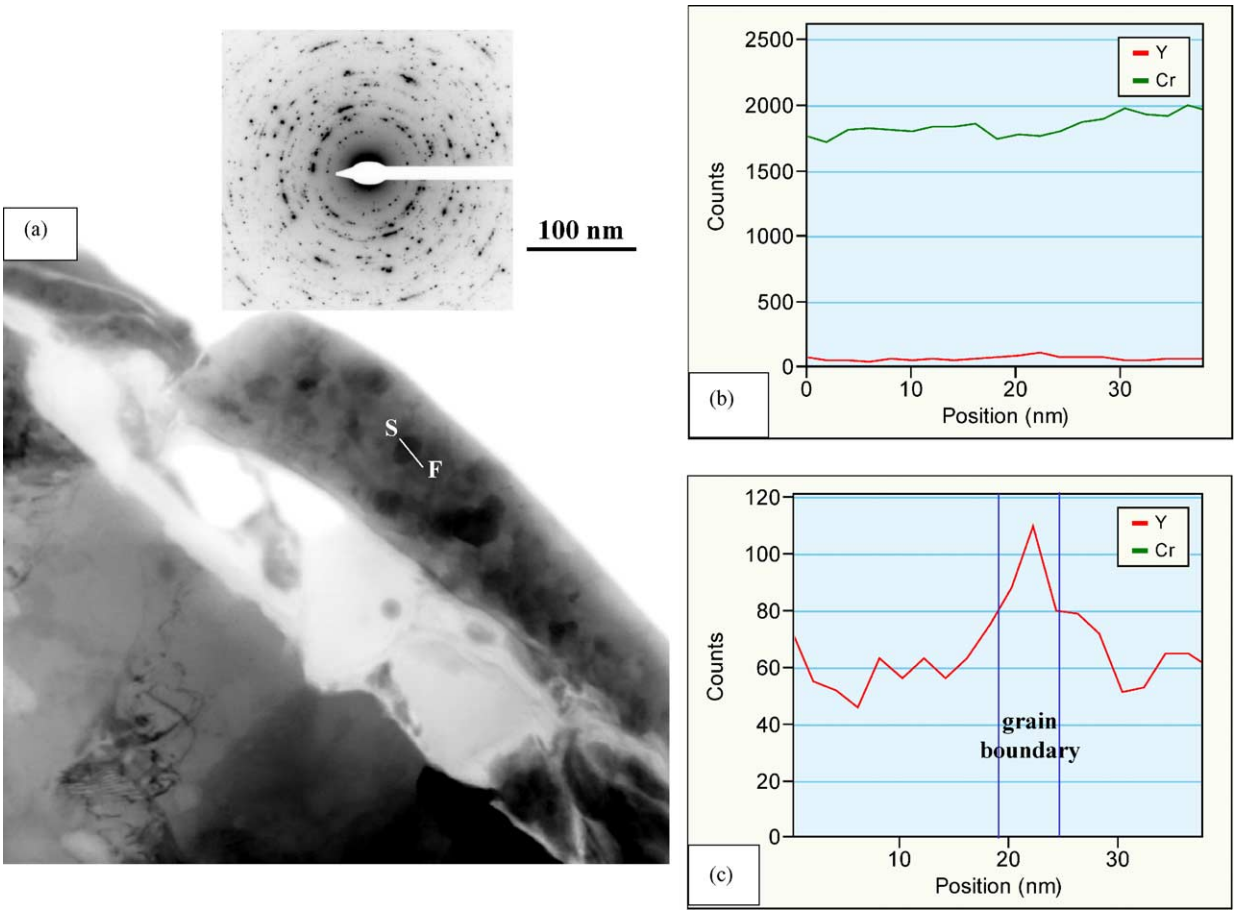

Fig. 13. (a) STEM image from Y/Co sample annealed for 500 h showing the Cr_2O_3 layer along with accompanying SAD pattern. (b) X-ray linescan across two Cr_2O_3 grains indicated in (a), showing distribution of Cr and Y. (c) Yttrium X-ray linescan from (b) magnified to show Y enrichment at the grain boundary.

is much thicker in those locations and no Y or Co is present in the oxide. The scratched regions, i.e., missing the Y/Co coating, account for the variable thickness visible in Fig. 12.

A comparison of the three types of samples, after annealing for 1000 h, is shown in Fig. 16. Both rare earth elements, Y and Ce, decrease the oxide growth rates relative to the uncoated steel, with Y being more effective (oxide growth is reduced by a factor of 3 at 750 °C). In both coated samples, Co is primarily present in the spinel phase; any doping effect in Cr_2O_3 is unclear at this time.

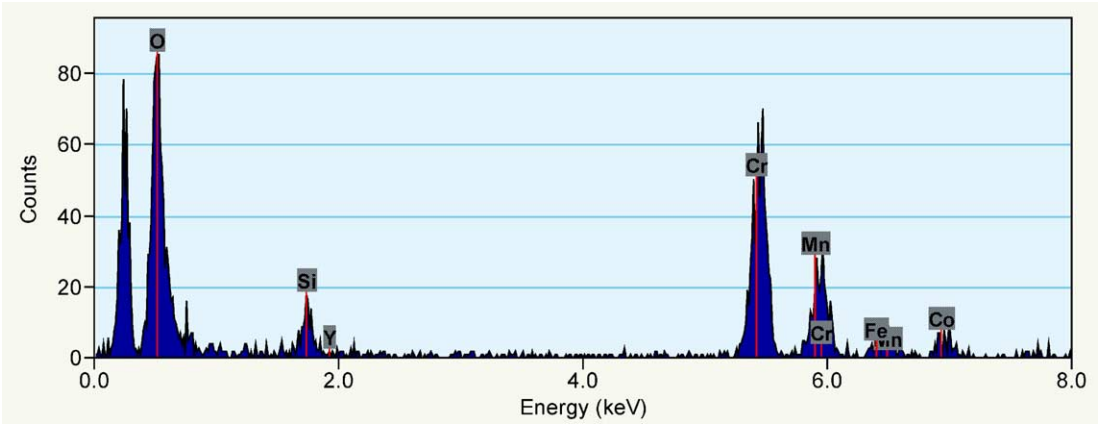

Fig. 14. EDX spectrum from a spinel particle of an Y/Co sample annealed for 500 h. Note the presence of Co and the absence of Y.

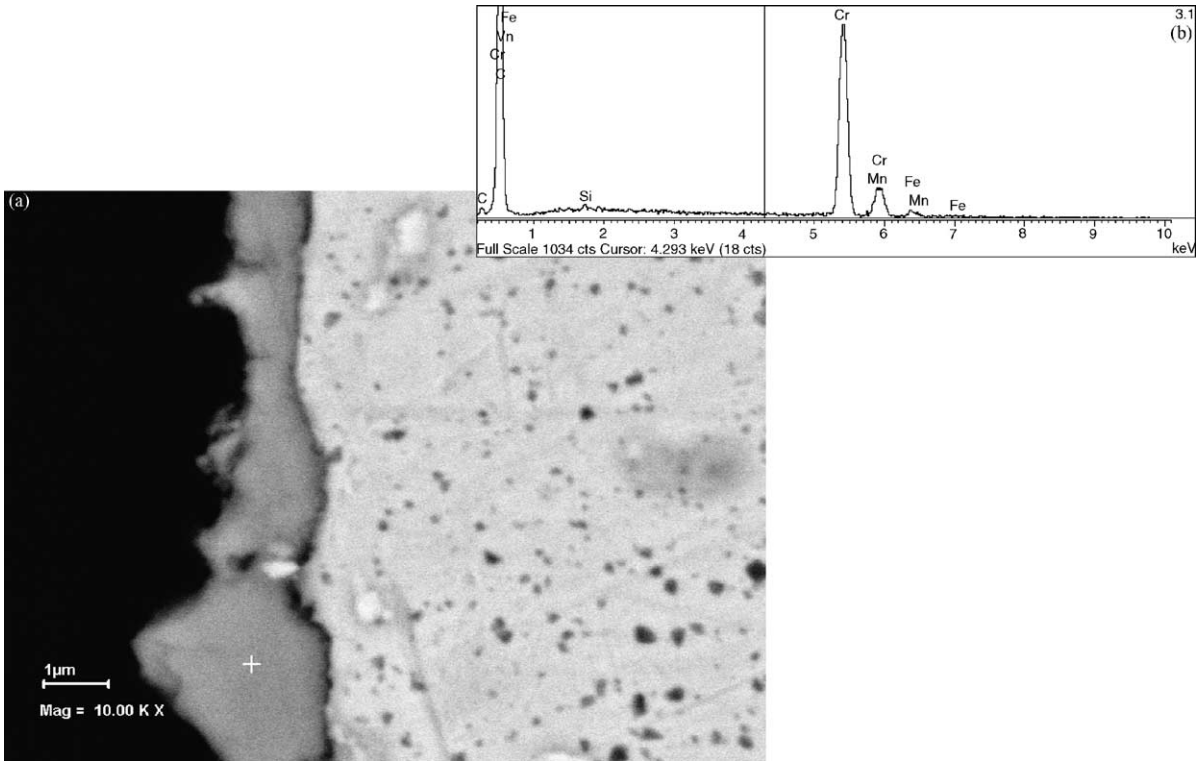

Fig. 15. (a) SEM BSE image from Y/Co sol–gel sample, where coating has been removed prior to annealing. (b) EDX spectrum from inner oxide layer.

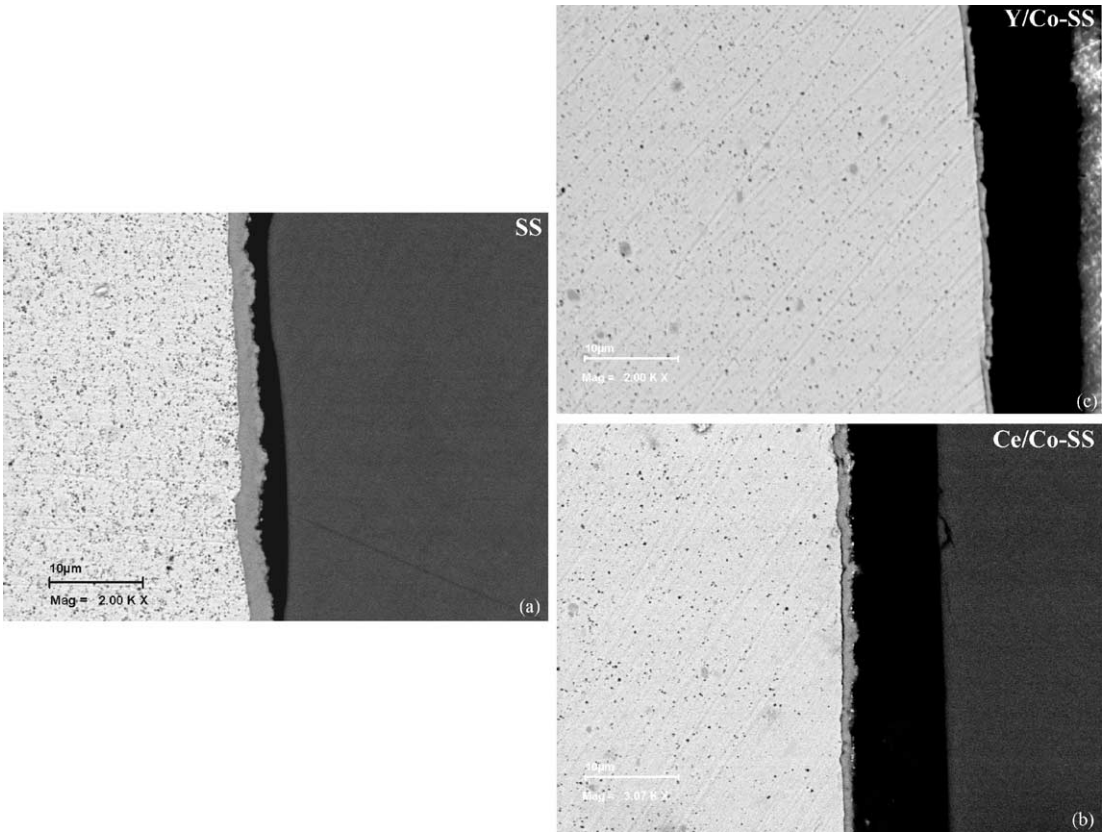

Fig. 16. SEM BSE from samples annealed for 1000 h. (a) uncoated stainless steel; (b) Ce/Co coated steel; (c) Y/Co coated steel.

4. Summary

Sol–gel coatings, containing either Ce/Co or Y/Co and each ~200 nm thick, were deposited onto ferritic stainless steel coupons in an effort to improve oxidation resistance in solid oxide fuel cell environments. Both types of coatings exhibited lower rates of oxidation relative to the uncoated steel, with the Y/Co coating yielding the best results. Cr_2O_3 layer thicknesses, after annealing in air for 1000 h, were <1 μm for Y/Co coated samples, between 1.0 and 1.5 μm for Ce/Co coated samples and close to 3 μm for the uncoated steels. For Ce/Co coatings, Ce was present as distinct CeO_2 particles at the Cr_2O_3/spinel interface. For the Y/Co coated samples, no distinct Y-rich phases were identified; Y was dissolved within the Cr_2O_3 phase with higher levels at the grain boundaries. Cobalt in both Ce/Co and Y/Co coatings was primarily present in the spinel phase.

Acknowledgements

Research funding was provided by the Core University Research in Sustainable Energy (COURSE) Program sponsored by the Alberta Energy Research Institute (AERI). The authors wish to thank J. Protkova (Fuel Cell Energy) for her assistance with the SEM analysis.

References

[1] H. Yokokawa, N. Sakai, T. Horita, K. Yamaji, Fuel Cells 1 (2001) 117.
[2] T. Brylewski, M. Nanko, T. Maruyama, K. Przybylski, Solid State Ion. 143 (2001) 131.
[3] J.M. Ralph, A.C. Schoeler, M. Krumpelt, J. Mater. Sci. 36 (2001) 1161.
[4] S.P.S. Badwal, Solid State Ion. 143 (2001) 39.
[5] A.V. Virkar, D.M. England, Solid State Fuel Cell Interconnector, United States Patent 6,054,231 (25 April 2000).
[6] G.V. Samsonov (Ed.), The Oxide Handbook, IFI Plenum, New York, 1973.
[7] K. Huang, P.Y. Hou, J.B. Goodenough, Mater. Res. Bull. 36 (2001) 81.
[8] W.H. Zhu, S.C. Deevi, Mater. Res. Bull. 38 (2003) 957.
[9] R. Haugsrud, Corros. Sci. 44 (2002) 1569.
[10] M.J. Capitan, A. Paul, J.L. Pastol, J.A. Odriozola, Oxid. Met. 52 (1999) 447.
[11] F. Riffard, H. Buscail, E. Caudron, R. Cueff, C. Issartel, S. Perrier, Mater. Character. 49 (2002) 55.
[12] X.G. Zheng, D.J. Young, Corros. Sci. 40 (1998) 741–756.
[13] F. Riffard, H. Buscail, E. Caudron, R. Cueff, C. Issartel, S. Perrier, Appl. Surf. Sci. 199 (2002) 107.
[14] A.I. Saprykin, J.S. Becker, U.V.D. Crone, H.-J. Dietze, Fresenius J. Anal. Chem. 358 (1997) 145.
[15] D.A. Downham, S.B. Shendye, Oxid. Met. 43 (1995) 411.